RSC Advances

PAPER

View Article Online
View Journal | View Issue

Cite this: *RSC Adv.*, 2016, **6**, 106732

On the agent role of Mn^{2+} in redirecting the synthesis of $Zn(OH)_2$ towards nano-ZnO with variable morphology†

Daniela Ghica,* Ioana D. Vlaicu,* Mariana Stefan, Leona C. Nistor and Sergiu V. Nistor

Received 15th September 2016
Accepted 2nd November 2016

DOI: 10.1039/c6ra23065b

www.rsc.org/advances

One of the simplest routes to prepare polycrystalline $Zn(OH)_2$ is by coprecipitation, with zinc nitrate as a cation source. However, the addition of even minute amounts of manganese nitrate to the precursors used to prepare pure $Zn(OH)_2$ results in Mn^{2+} doped nanostructured ZnO. The comparison with other Mn^{2+} doped metal hydroxides prepared by the same coprecipitation method, involving metal nitrates precursors, shows that this behavior is unique, pertaining only to $Zn(OH)_2$. A systematic study of the samples prepared without and with variable amounts of Mn^{2+} ions, in the 1 to 5000 ppm nominal concentrations range showed that the re-routing of the reaction takes place even for the lowest nominal dopant concentration of 1 ppm. According to X-ray diffraction, transmission electron microscopy and Fourier transform infrared spectroscopy investigations, both crystallite size and morphology of the resulting nanostructured ZnO samples varied with the Mn^{2+} nominal concentration. Moreover, quantitative electron paramagnetic resonance investigations showed that the incorporation rate of the Mn^{2+} ions at different sites in the nanostructured ZnO depended on the nominal Mn^{2+} concentration. The results are discussed in terms of the coordination properties of the Mn^{2+} and Zn^{2+} ions and the nature of the reaction precursors.

1. Introduction

Doped nanocrystalline zinc oxide (nano-ZnO) is one of the most studied semiconductors, many investigations being focused on tailoring the material properties for applications in spintronics, nano- and/or optoelectronics, by changing/adjusting the nature and concentration of the dopant ions.[1–4] Doping nanocrystals, typically grown using colloidal synthesis, is still an experimental challenge and the progress in controlling and understanding the incorporation of impurities in semiconductor nanocrystals has been slow.[5–7] Thermally induced decomposition of doped precursors has proved to be an alternative efficient way to obtain doped nano-ZnO. Thus, as shown in the case of the Mn^{2+} doped hydrozincite (ZCB) – $Zn_5(CO_3)_2(OH)_6$ precursor, with proper adjustment of the annealing temperature and atmosphere conditions it was possible to control the size and size distribution of the resulting Mn^{2+} doped ZnO (ZnO:Mn) nanoparticles.[8,9]

Zinc hydroxide – $Zn(OH)_2$ has attracted a lot of interest during the last years as a precursor in the synthesis of nano-ZnO with controlled size and morphology.[10–14] Moreover, as in the case of the ZCB,[8,15] doped $Zn(OH)_2$ was expected to be also a valuable precursor for doped nano-ZnO. However, our attempts to prepare $Zn(OH)_2$ by coprecipitation in the presence of Mn^{2+} ions failed to produce the expected Mn^{2+} doped $Zn(OH)_2$.[13] Every sample prepared in these conditions resulted in nano-ZnO:Mn, independent of the Mn^{2+} ions concentration. To our knowledge, this is the first observation of a redirection of the $Zn(OH)_2$ synthesis towards nano-ZnO by doping instead of by modifying essential synthesis or post-synthesis parameters (*i.e.* temperature, pressure, stirring), as previously reported (*e.g.* ref. 10–14 and 16).

In an effort to understand the extent of the manganese effect on the reaction products and to determine the Mn^{2+} concentration threshold for the synthesis redirection to take place, we performed a systematic study of the samples prepared without and with a Mn^{2+} source, varying the nominal Mn^{2+} ions concentration from 1 to 5000 ppm. Structural and morphological studies have been performed by X-ray diffraction (XRD), transmission electron microscopy (TEM) and Fourier transform infrared (FTIR) spectroscopy. The localization and distribution of the Mn^{2+} ions in the $Zn(OH)_2$ and ZnO samples were determined by multifrequency electron paramagnetic resonance (EPR) spectroscopy, which we successfully employed to investigate various Mn^{2+} doped semiconducting nanostructures.[8,9,13,17–19] We have shown that EPR spectroscopy is a sensitive and reliable, statistically relevant technique (as it

National Institute of Materials Physics, Atomistilor Str. 405A, Magurele, 077125, Romania; Web: http://www.lab50.infim.ro; http://www.cetresav.infim.ro. E-mail: ghica@infim.ro; ioana.vlaicu@infim.ro; Fax: +40 21 3690177; Tel: +40 21 2418108; +40 21 2418290

† Electronic supplementary information (ESI) available. See DOI: 10.1039/c6ra23065b

measure the whole volume of the sample), which can offer accurate information concerning the localization of the paramagnetic Mn^{2+} ions in the volume and at the surface/interface of the nanostructures, the configuration of their neighboring ligands and the local structural/bonding modifications induced by thermo-chemical treatments.

The discussion of the results takes into consideration the role played by the Mn^{2+} and Zn^{2+} ions, their favored coordination and the nature of the reaction precursors in redirecting the $Zn(OH)_2$ synthesis towards nano-ZnO.

2. Experimental section

2.1. Synthesis

The starting materials used in the synthesis were analytical grade zinc nitrate hexahydrate ($Zn(NO_3)_2 \cdot 6H_2O$ – 99% purity), manganese nitrate tetrahydrate ($Mn(NO_3)_2 \cdot 4H_2O$ – 99.98% purity) and sodium hydroxide (NaOH – 97% purity) from Alfa Aesar, without further purification. Pure crystalline $Zn(OH)_2$ was prepared by coprecipitation of an aqueous solution of zinc nitrate with sodium hydroxide (in excess) by a procedure described elsewhere.[13] The syntheses in the presence of Mn^{2+} ions were made by a similar procedure, which consisted in mixing the corresponding amounts of 0.19 M $Zn(NO_3)_2$ and 0.02 M $Mn(NO_3)_2$ aqueous solutions at 50 °C to obtain Mn/Zn ratios of 1, 5, 50, 100, 500, 1000 and 5000 ppm (0.5 at%). Afterwards, an aqueous solution of 2.4 M NaOH was added dropwise using a peristaltic pump under continuous stirring. The resulting precipitates were then centrifuged, washed several times with bi-distilled water and finally with absolute ethanol and dried at 60 °C (in air) in a similar way as the pure $Zn(OH)_2$.

In order to ascertain the role of the precursor materials in the reactions leading to the final product, several other compounds were synthesized by the same procedure. Thus, to investigate the role of the Zn^{2+} ions in obtaining ZnO:Mn instead of Mn^{2+} doped $Zn(OH)_2$, other metal hydroxides such as $Mg(OH)_2$, $Ca(OH)_2$ and $Cd(OH)_2$ were synthesized in both pure and manganese doped forms, with Mn^{2+} nominal concentrations of 1000 ppm. Also, taking into account the possibility that the anionic part of the precursors (*i.e.* the nitrate) may be responsible for the observed turn of the reactions, several syntheses were performed starting from M(II) chlorides/acetates (where M(II) = Zn^{2+} and Mn^{2+}).

2.2. Characterization methods

XRD investigations were performed with a Bruker D8 Advance X-ray diffractometer, in the θ–θ geometry, with Cu anode and Ni filter (λ = 1.54184 Å). The lattice parameters of the identified crystalline phases and the average crystallites size were determined by Rietveld refinement of the experimental data using the Topas v. 3 software from Bruker.

TEM/HRTEM morphology and structure investigations at low and high magnifications were performed with an atomic resolution analytical JEOL ARM 200F electron microscope operated at 200 kV, on specimens prepared by crushing the as grown powder in ethanol, dispersing it by sonication, dropping it on lacey carbon grids and drying it at room temperature (RT).

Weighted amounts of pure and Mn doped powdery samples were inserted in calibrated pure fused silica EPR sample tubes of 2 mm and 3 mm inner diameter. The X (9.5 GHz)- and Q (34 GHz)-band EPR measurements were performed at RT with the Bruker ELEXSYS-E580X and -E500Q spectrometers, respectively, from the Center for advanced ESR/EPR techniques (CetRESav – http://www.cetresav.infim.ro/). The X-band spectrometer, equipped with the calibrated Super High QE cylindrical cavity resonator (ER 4123SHQE), was also employed for quantitative determinations of the Mn^{2+} ions concentration in the investigated samples. The absolute spin quantitation routine (based on the double integration of the spectra), included in the XEPR software from Bruker, was used. The spin Hamiltonian (SH) parameters of the observed paramagnetic centers were determined using a two-steps procedure[20] based on the lineshape simulation of the EPR spectra with the EASYSPIN v.5.0.12 software.[21]

FTIR spectra were recorded on several selected samples with a Spectrum BX II (Perkin Elmer) spectrometer in the 4000–350 cm^{-1} spectral range, with 128 scans and 4 cm^{-1} resolution. The ZnO:Mn samples were embedded/diluted in KBr pellets.

3. Results and discussion

3.1. XRD results

The XRD pattern of the undoped sample (Fig. 1 – bottom) shows the presence of a single phase ε-$Zn(OH)_2$ with orthorhombic ($P2_12_12_1$) structure [JCPDS card no. 38-0385]. The resulting lattice parameters (Table S1 from ESI†) are similar with those previously reported.[13]

In the case of the Mn^{2+} doped samples, the analysis of the XRD patterns evidences the formation of a single phase of nanocrystalline hexagonal ZnO [JCPDS card no. 89-1397] in all samples, even for the lowest Mn^{2+} nominal concentration of 1 ppm. Fig. 1 presents only the XRD patterns of the samples

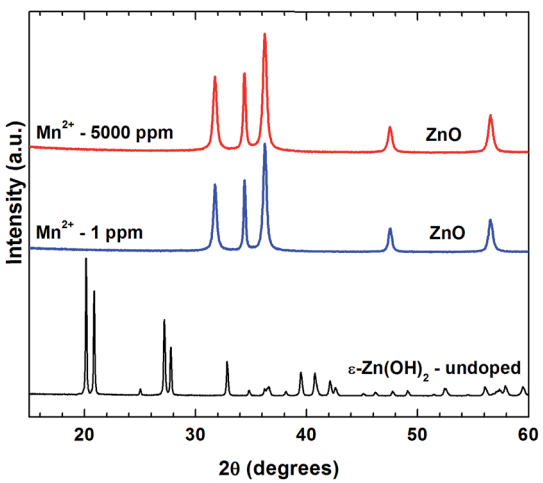

Fig. 1 XRD diffractograms of the undoped (bottom) and Mn^{2+} doped (upper) samples.

with the minimum and maximum Mn^{2+} nominal concentration. The resulting ZnO crystallite sizes and lattice parameters for all investigated samples are presented in Table S1 from ESI.† The values are similar for all samples in the 1–1000 ppm nominal concentration range, with notable changes observed only for the sample with the maximum Mn^{2+} nominal concentration of 5000 ppm: the average crystallite size decreases from 38 nm to 32 nm.

The substitution of the tetrahedrally coordinated Zn^{2+} ions (Shannon-Prewitt crystal radius RSP = 0.74 Å (ref. 22)) by the larger Mn^{2+} ions (RSP = 0.80 Å (ref. 22)) produces an expansion of the ZnO lattice associated to lattice disorder. This is evidenced by the changes observed in the XRD parameters, namely an increase of the lattice parameters and a decrease of the crystallite size. Such results have been also reported for other Mn doped ZnO nanostructures (see ref. 18 and references cited therein). If the Mn concentration is lower than 1%, as in our case, the effect is relatively reduced, as presented in Table S1 – ESI.†

There are several mechanisms proposed to explain the inhibition of the ZnO crystallites growth by the presence of impurities.[23–25] The reduced diffusivity in ZnO due to Zn concentration decrease in the doped samples suppresses the grain growth. Also, the presence of impurities produces a retarding force on the grain boundaries, impeding the grain growth. Moreover, in Al doped ZnO the grain growth activation energy was determined to increase in the presence of impurities.[24] All these would contribute to a gradual decrease of the grain size with the increase of the impurities concentration.

3.2. TEM investigations

TEM images of the undoped $Zn(OH)_2$ sample (see Fig. S1 from ESI†) revealed the plate-like, rod-like morphology of the crystallites of rather large (100–1200 nm) dimensions. The corresponding electron diffraction patterns were indexed with the ε-$Zn(OH)_2$ phase. On the other hand, when the preparation of Mn^{2+} doped $Zn(OH)_2$ was attempted by the same procedure, the nature/structure of the obtained precipitate changed in a rather drastic way. As shown by X-ray (Fig. 1) and electron diffractions (Fig. 2), even at the smallest (1 ppm) Mn^{2+} nominal concentration, the ZnO phase was formed instead of $Zn(OH)_2$.

The TEM images in Fig. 2 illustrate the changes in the morphology of the resulting ZnO samples doped with Mn^{2+} ions of increasing nominal concentrations. According to Fig. 2a the sample prepared with 1 ppm Mn^{2+} nominal concentration consists of large nanoparticles (30–200 nm), most of them with lamellar and rod shapes. It is interesting to note that the pure $Zn(OH)_2$ sample exhibits the same morphology, but the crystallites are much larger (one order of magnitude on the average). In the case of the sample prepared with 1000 ppm

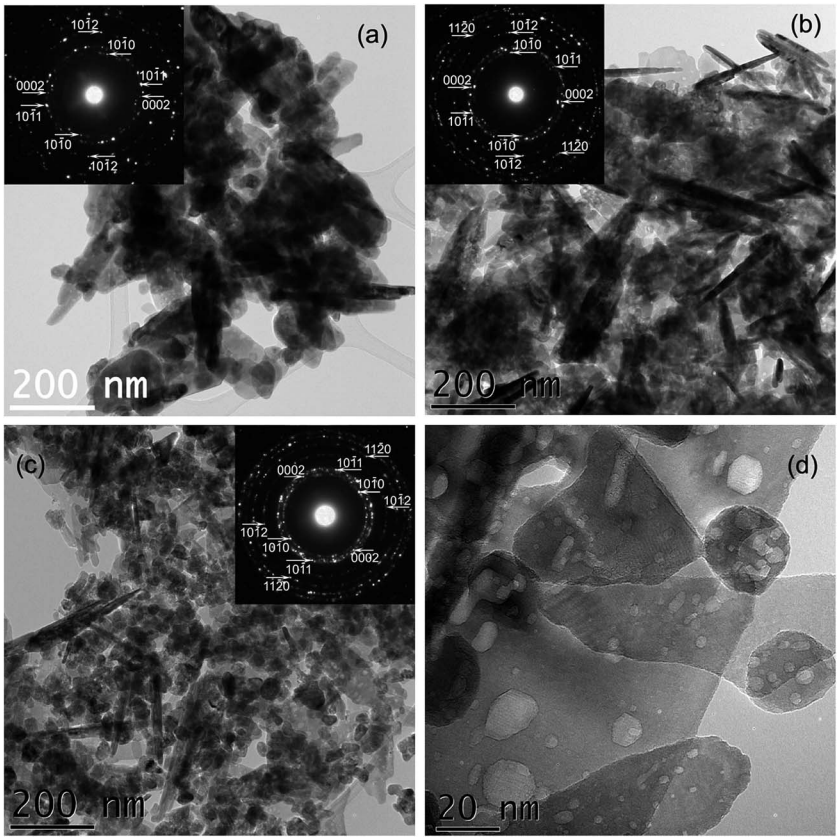

Fig. 2 TEM/HRTEM images and the corresponding ED patterns (insets) for the ZnO samples doped with 1 ppm (a), 1000 ppm (b), 5000 ppm (c) Mn^{2+} nominal concentration. (d) HRTEM image at larger magnification of the sample with Mn^{2+} 5000 ppm nominal concentration. The ED patterns were indexed with the ZnO structure.

Mn^{2+} nominal concentration (Fig. 2b) the lamellar nanoparticles are smaller, while the rods remain of the same size as in the sample prepared with 1 ppm Mn^{2+}.

Finally, in the case of the sample prepared with 5000 ppm Mn^{2+} nominal concentration, Fig. 2c shows that the majority of the nanoparticles exhibits a rather uniform morphology with smaller, 20–60 nm size, although some nanorods and lamellar nanoparticles are still present. Therefore, the increase in the Mn^{2+} nominal concentration leads to the formation of ZnO nanoparticles with much more uniform morphology and smaller dimensions. All the corresponding electron diffraction (ED) patterns in the insets of Fig. 2a–c were indexed with the ZnO structure. The HRTEM image (Fig. 2d) reveals additional details of the sample prepared with 5000 ppm nominal concentration of Mn^{2+} ions. The morphology of the nanocrystals is indeed polyhedral. Voids with dimensions of 1–16 nm are observed on each nanocrystallite. It looks like a degassing effect took place during their synthesis. Note that the presence of these voids can be also observed in Fig. 2a, in regions where the large crystallites are not overlapped, suggesting that their presence is not related to an increase in the nominal concentration of Mn^{2+} ions in the solution, but to the synthesis process itself. These voids were observed only in the Mn^{2+} doped nano-ZnO, independent of the Mn concentration, and not in the undoped $Zn(OH)_2$, as one can see in Fig. S1 from ESI.†

3.3. EPR results

3.3.1. Mn^{2+} paramagnetic centers. Fig. 3 presents the Q-band EPR spectra of selected samples, showing significant differences. Each spectrum was recorded in the multiscan mode, increasing the number of scans at 0.16 mW microwave power and 1 G modulation amplitude values from 1 up to 100 scans, from the maximum to the minimum Mn^{2+} nominal concentrations, respectively, in order to enhance the signal to noise ratio. The EPR spectra were further normalized to the same amplitude of the Mn^{2+}(c) center spectrum (Fig. 3), to better follow the lineshape changes.

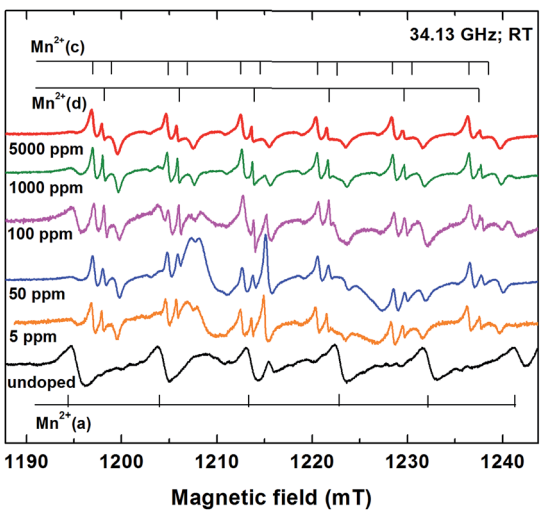

Fig. 3 Multiscan Q-band EPR spectra for the undoped (bottom) and Mn^{2+} doped (upper) samples. The six hyperfine lines/doublet-lines of the Mn^{2+}(a), Mn^{2+}(d)/Mn^{2+}(c) paramagnetic centers are marked with vertical bars.

The EPR spectrum of the undoped sample (Fig. 3 – bottom), recorded with 100 scans, corresponds to paramagnetic impurity levels of less than 1 ppm. It consists of a dominant set of six lines with almost equal intensity, separation (~9.2 mT) and linewidth, characteristic for the central hyperfine allowed (M_s: $-1/2 \leftrightarrow 1/2$, $\Delta M_I = 0$) transitions of the Mn^{2+} ions ($S = 5/2$, $I = 5/2$) in a polycrystalline lattice host.[20] A few additional lines from other paramagnetic defects are also present in the EPR spectrum, as previously reported.[13]

The EPR spectra of the Mn^{2+} doped samples differ from the EPR spectrum of the undoped sample, due to the different host lattice. These spectra are dominated by six similar groups of three close lying lines, with a ~7.8 mT separation between the groups, typical for Mn^{2+} in ZnO.[26] Another sextet of lines, with a larger ~9 mT separation, belonging to a different Mn^{2+} center, can be observed. The relative intensities of the two sextets are different in the five different Mn^{2+} doped samples (Fig. 3).

The SH parameters of the Mn^{2+} centers, determined by simulation and lineshape fitting of the X- and Q-band spectra of the undoped and doped samples, are given in Table S2 from ESI.† In the undoped sample the SH parameters of the paramagnetic center called Mn^{2+}(a) are identical with those previously reported for the substitutional Mn^{2+} ions in $Zn(OH)_2$.[13] The localization of the Mn^{2+} in the ε-$Zn(OH)_2$ lattice at tetrahedrally, four-fold coordinated Zn^{2+} cation sites resulted from the analysis of the multifrequency EPR spectra, recorded on as grown and annealed polycrystalline ε-$Zn(OH)_2$.[13] One could thus explain why during the thermal decomposition of the polycrystalline ε-$Zn(OH)_2$ into nano-ZnO, the observed paramagnetic Mn^{2+} centers transformed into Mn^{2+} centers consisting of Mn^{2+} ions localized substitutionally at Zn^{2+} sites in the ZnO lattice.[13] The substitutional localization of the Mn^{2+} impurity ions in ε-$Zn(OH)_2$ at Zn^{2+} cation sites fourfold coordinated by hydroxyl ligands was further confirmed by the observed changes in the Mn^{2+} ions hyperfine splitting during the three-steps thermal decomposition of the ε-$Zn(OH)_2$ shell of cubic ZnS nanocrystals with core–shell structure into a ZnO shell.[19] The hyperfine splitting changes reflected the sequential dehydration of the four nearest neighbor hydroxyl ligands.

The complex sextet in the EPR spectrum of the Mn^{2+} doped samples is generated by two types of Mn^{2+} paramagnetic centers, called Mn^{2+}(c) and Mn^{2+}(d) (see Fig. 3 and 4). Their SH parameters (Table S2 – ESI†) are very close to those previously reported for the Mn^{2+}-c and Mn^{2+}-d centers in the nanostructured ZnO resulted from the thermal decomposition of ZCB,[8] which consist of Mn^{2+} ions substitutionally localized at tetrahedrally coordinated Zn^{2+} sites in ZnO nanocrystals and disordered ZnO phase, respectively. The very small differences (less than 2%) in the hyperfine parameters of the Mn^{2+} centers localized in ZnO (see Table S2 – ESI†) can be explained by slightly different average coordination numbers of the Mn^{2+} ions,[9,27] associated with small variations in samples stoichiometry. Such variations could appear due to the particularities of the synthesis routes.

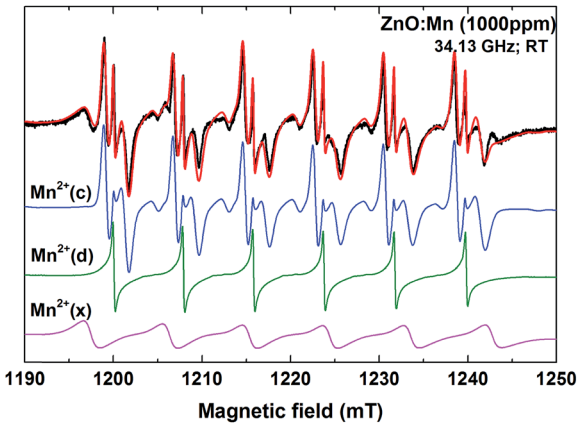

Fig. 4 Experimental (black) and simulated (red) Q-band EPR spectrum of the ZnO sample with 1000 ppm Mn^{2+} nominal concentration. Contributions to the simulated spectrum of the Mn^{2+} ions localized in crystalline (Mn^{2+}(c) – blue) and disordered (Mn^{2+}(d) – green) ZnO environment, and in the unknown disordered phase (Mn^{2+}(x) – magenta) are shown below.

The third Mn^{2+} center in the EPR spectrum of the Mn^{2+} doped samples, with larger hyperfine separation, called Mn^{2+}(x) (Fig. 4), is better observed in the EPR spectrum of the sample with 100 ppm Mn nominal concentration (see Fig. 3). The SH parameters of the Mn^{2+}(x) center, presented in Table S2 from ESI,† indicate the localization of the Mn^{2+} ions in a disordered environment, different from ZnO.

3.3.2. Quantitation of the Mn^{2+} paramagnetic centers. The absolute number of spins in each doped nano-ZnO sample was determined by the quantitation of the X-band EPR spectra recorded for weighted amounts of the samples. The resulting spin concentrations correspond to the total concentrations of Mn^{2+} ions in the samples. In order to determine the distribution of the Mn^{2+} ions at different sites, the X- and Q-band EPR spectra were submitted to deconvolution procedures, thus separating the component spectra corresponding to the different centers. As an example, the deconvolution of the Q-band EPR spectrum of the sample with 1000 ppm Mn^{2+} nominal concentration is shown in Fig. 4.

The evolution of the concentrations of the three Mn^{2+} centers with the nominal concentration increase, as determined from the deconvoluted spectra, is presented in Table 1.

Unsurprisingly, the total concentration of incorporated isolated Mn^{2+} ions is much lower than the nominal concentration, in agreement with the low doping efficiency observed in Mn doped II–VI nanostructures.[6,7,28–31] For the samples with nominal concentrations lower than 100 ppm the low incorporation efficiency resulted in very low intensity X-band spectra, and, therefore, in unreliable quantitation results.

One can notice that the percentage of Mn^{2+}(c) centers from the total concentration C_t of isolated Mn^{2+} ions in the sample increases as the Mn^{2+} nominal concentration increases. This behavior seems to be correlated with the morphology changes observed by TEM *vs.* Mn^{2+} nominal concentration increase, in agreement with theoretical studies which show that the doping efficiency varies with the morphology and size of nanocrystals.[5,32]

Assuming a uniform distribution of the Mn^{2+} ions in the sample material, the relative concentrations of the three paramagnetic centers would reflect the proportions of their host structural phases in the sample volume. According to the data in Table 1, the concentration of the Mn^{2+}(x) centers is quite high in all samples, which would correspond to the presence of a large amount of the unknown disordered X phase in the samples. However, no trace of such a secondary phase has been detected by XRD (Fig. 1) or TEM (Fig. 2), meaning that the amount of the disordered X phase is below the detection limit (1–2%). Therefore one concludes that the Mn^{2+} ions distribution is not uniform in the sample and that the considerably large percentage of Mn^{2+} ions localized in the disordered phases reflects a segregation process of the Mn^{2+} ions outside the ZnO nanocrystals. This segregation process diminishes as the nominal concentration of Mn^{2+} ions increases.

3.4. FTIR measurements

The FTIR spectra recorded for the manganese doped ZnO samples (with 1, 50, 1000, and 5000 ppm Mn nominal concentrations) exhibit similar features, with small differences related to the intensities and positions of certain absorption bands (Fig. 5). The sharp and very intense absorption bands in the 560–400 cm^{-1} spectral range correspond to the presence of a dominant ZnO phase. The positions and number of these absorption bands, characteristic to the ν(Zn–O) stretching vibration modes, depend on the particles morphology.[33,34] Thus, spherical ZnO particles usually show a single distinct IR absorption band, while for ZnO particles with different

Table 1 Concentrations of the three Mn^{2+} paramagnetic centers (in ppm and % of the total concentration C_t of incorporated Mn^{2+} ions) in doped ZnO samples[a]

Mn^{2+} nominal concentration	C_t [ppm]	Mn^{2+}(c) concentration		Mn^{2+}(d) concentration		Mn^{2+}(x) concentration	
		[ppm]	[% C_t]	[ppm]	[% C_t]	[ppm]	[% C_t]
100 ppm	4	1	25	0.5	13	2.5	62
500 ppm	18	5	29	4	22	9	49
1000 ppm	26	11	44	5	19	10	37
5000 ppm	49	25	50	8	16	16	34

[a] The error was estimated to be 25–30%.

morphologies this band splits in characteristic ways.[33,34] Following the profiles of these IR bands in Fig. 5, one can notice that, by increasing the Mn nominal concentration, the positions, number and intensities of the ν(Zn–O) bands change in agreement with the morphologic changes of the nanostructured ZnO phase, from the dominant lamellar towards the dominant polyhedral shape. These variations in the nanostructured ZnO morphology with the Mn doping concentration, reflected in the FTIR spectra, are in agreement with the TEM results.

Several medium to weak intensity absorption bands observed in the 1460–760 cm^{-1} spectral range, assigned to the vibration modes for nitrate ions (NO_3^-), indicate the presence of a secondary phase which contains nitrate groups in its chemical composition.[35] The vibration modes observed at ~3420 cm^{-1} and ~1640 cm^{-1} are attributed to the presence of hydroxyl ions, which can originate from adsorbed water or a hydroxide compound.[36] The FTIR results are in agreement with the EPR data, confirming the coexistence in these samples of a dominant ZnO phase (nanocrystalline + disordered) and a secondary X phase (disordered) which, according to FTIR data, is expected to contain nitrate groups. Such a secondary phase could be incorporated between the aggregated ZnO nanoparticles during the final drying step, similar to the case of the cZnS nanoparticles synthesis.[37] Table S3 from ESI† summarizes the most important absorption bands maxima observed in the infrared spectra and their assignments for the investigated ZnO:Mn samples.

Although the change in the morphology of the nanostructured ZnO with increasing Mn^{2+} concentration, observed by TEM and FTIR, is not a new phenomenon, a recently published review[38] regarding the influence of ionic impurities on the phase and growth/morphology of semiconductor nanocrystals shows that, despite intensive research, there are fundamental issues still unsolved. Previous articles have reported morphological changes of the ZnO nanomaterials associated with the doping process,[39–43] which could be connected to specific structural and coordination properties, as further explained. The crystallographic plane with the minimum surface free energy determines the preferential growth direction. For semiconductors, the surface free energy depends on the hybridized orbit. In the tetrahedrally coordinated (sp^3 hybridized orbit) ZnO, with wurtzite structure, the (001) plane has the minimum surface free energy, resulting in a preferential growth along the *c*-axis, *i.e.* a (001) "self-texture".[44] The impurities, once added, become involved in the nucleation and growth processes, influencing thus the surface free energy and therefore the morphology and size of a given crystallite. For example, doping induced morphology changes were reported in the case of the ZnO nanorods, with the different shapes depending on the nature of the impurities: better-formed nanorods (Li, Na doped ZnO), petal-like particles (Mg doped ZnO), both rods and irregular shaped particles with a tendency to agglomeration (Cu doped ZnO), spherical particles (Pr^{3+} doped ZnO).[39] Moreover, doping with Fe^{3+} ions was reported to induce important changes in the morphology of nanostructured ZnO, ranging from nanowires to nanorods and then to nanoparticles, only by increasing the dopant concentration.[41] Also, in Ni/Fe mono- or co-doped ZnO nanomaterials, the morphology changed from highly crystalline nanorods at low dopant concentration (<5%) towards well dispersed plate-like nanoparticles at higher dopant concentration.[42] The explanation offered for these effects was that the replacement of the Zn^{2+} ions by Fe^{2+}/Ni^{2+} ions could affect the local charge density, polarity and potential energy of specific crystal planes, thus resulting in changes of the growth orientation with the Fe/Ni dopant concentration increase.[42]

Yang *et al.*[40] have shown that ZnO faceted nanocrystals changed into nano-tetrapods when doped with a few percent of divalent Mg, Cd, Ni or Mn ions. At high doping concentrations (>30%), the tetrapods changed into nanowires. They experimentally found that the dopants play an important role in the primary growth stage, resulting in initial growth seeds with diverse crystallographic structures, which are critical for the generation of doped nanocrystals with different shapes. Further investigations dedicated to Mn doped nano-ZnO[45] explored the growth mechanism of doped ZnO with an interesting shape transition from tetrapods to spherical nanoparticles by increasing the reaction time and temperature, without changing the dopant concentration. However, it was shown[38,40,45] that the growth mechanism is not simple and further experiments and theoretical simulations are required for specific growth conditions.

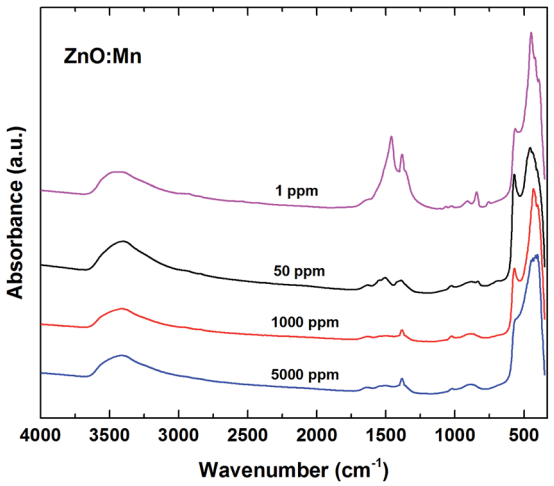

Fig. 5 FTIR spectra for ZnO:Mn samples doped with 1, 50, 1000, and 5000 ppm Mn nominal concentration.

3.5. Comparison with metal hydroxides prepared by the same method

The most interesting and surprising result of this work is the redirection of the $Zn(OH)_2$ synthesis towards nano-ZnO even for nominal concentrations of Mn as low as 1 ppm added in the synthesis. However, the manganese doping was successfully achieved in other hydroxide materials such as $Mg(OH)_2$, $Ca(OH)_2$, β-$Ni(OH)_2$,[46–49] without producing structural changes of the host lattice. EPR studies have been performed and the SH parameters of the Mn^{2+} paramagnetic centers were determined

in $Mg(OH)_2$ and $Ca(OH)_2$ single crystals (SC) doped with significant concentrations of Mn^{2+} ions. In contrast, the SH parameters of the Mn^{2+} centers in $Zn(OH)_2$ were determined only recently in polycrystalline $Zn(OH)_2$ containing traces of Mn^{2+} ions (<1 ppm).[13] Because the above mentioned results were obtained on doped crystals synthesized by different procedures than the one we used, we decided to prepare several metal hydroxides, pure and doped with Mn, in order to check for a similar redirection of the hydroxide synthesis towards oxide induced by the Mn presence. We used the same preparation procedure and precursors as for $Zn(OH)_2$, replacing the Zn nitrate with nitrates of Mg, Ca and Cd. Fig. 6 presents the XRD patterns of the undoped and Mn (1000 ppm) doped $Mg(OH)_2$, $Ca(OH)_2$ and $Cd(OH)_2$ samples thus obtained. The XRD diffractograms have been indexed with the $Mg(OH)_2$, $Ca(OH)_2$ and $Cd(OH)_2$ structures, according to the JCPDS card no. 86-0441, JCPDS card no. 87-0674 and JCPDS card no. 73-0969, respectively. It is obvious that doping with 1000 ppm Mn did not induce structural changes of the $Mg(OH)_2$, $Ca(OH)_2$ and $Cd(OH)_2$ lattices, unlike the case of $Zn(OH)_2$.

We have also investigated the possible influence of the anion nature in the starting materials, by replacing the M(II) nitrates with M(II) acetates and chlorides, where M(II) = Zn^{2+} and Mn^{2+}, and leaving the other parameters of the preparation algorithm unaltered. The synthesis performed in the same conditions using zinc acetate as starting material resulted in a hydroxycarbonate compound, while the one using zinc chloride lead to zinc oxide. On the other hand, there are synthesis conditions (temperature, pH) for which ZnO is obtained from all the precursors, *i.e.* containing nitrate, chloride, sulphate or acetate.[50–53]

The addition of the Mn source in the synthesis procedure did not affect the result in either case. However, as none of the four synthesis procedures performed (acetate/chloride precursors with/without manganese) resulted in $Zn(OH)_2$, they cannot shed light on the cause of the synthesis redirection observed for nitrate precursors. Therefore this forms a separate subject which can be further studied.

In the case of the other metal hydroxides, we have to take into consideration that zinc itself could be responsible for the observed effect. Indeed, as previously reported,[54–56] Zn^{2+} has a different behavior than the other metal ions regarding its preferred coordination number and ligands type. While $Mn(OH)_2$, $Mg(OH)_2$, $Ca(OH)_2$, $Cd(OH)_2$ and β-$Ni(OH)_2$ exhibit the same CdI_2 type crystal structure (hexagonal system), where each cation is surrounded by six anions forming a slightly compressed octahedron, in the case of $Zn(OH)_2$, the Zn^{2+} ion has a tetrahedral coordination, each cation being surrounded by four anions. This difference in the coordination behavior of Zn^{2+} compared to the other M(II) ions could lead to a change in the hydroxide host lattice when the Mn^{2+} ions enter in Zn^{2+} sites, thus leading to the formation of doped ZnO instead of doped $Zn(OH)_2$. A possible explanation is that by forcing the Mn^{2+} ions, which prefer an octahedral coordination in almost all compounds, to replace Zn^{2+} in tetrahedrally coordinated sites in the $Zn(OH)_2$ lattice, a coordinative hindrance appears for manganese. As the specific role played by Mn^{2+} is restricted only to $Zn(OH)_2$, it is obvious that the observed effect is based on a fine balance between the Zn^{2+} cation, nitrate anion and Mn^{2+} dopant, which makes it difficult to give a precise growth mechanism at this stage. The elucidation of the exact reactions which take place during the synthesis necessitates more in-depth/dedicated investigations. Moreover, in spite of extensive studies, it is difficult to propose a definite growth mechanism even for pure ZnO, since there are many factors (such as temperature, pH, water presence) affecting the reactions.[38,57]

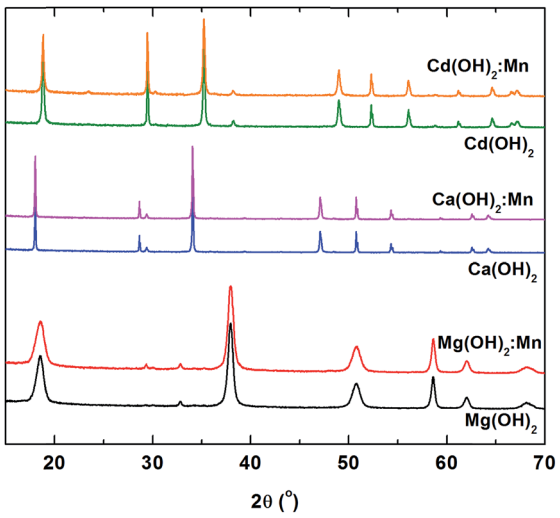

Fig. 6 XRD diffractograms of the pure and Mn (1000 ppm) doped $Mg(OH)_2$, $Ca(OH)_2$, and $Cd(OH)_2$ samples.

4. Conclusion

$Zn(OH)_2$ is one of the valued precursor materials which by a simple thermal annealing results in nanostructured ZnO with controlled size and size distribution. The attempt to add "controlled doping" to the properties of the resulting nano-ZnO lead us to the observation that the simple synthesis by coprecipitation method used for the envisaged Mn^{2+} doped $Zn(OH)_2$ was redirected and the final product was nano-ZnO:Mn. To our knowledge this is the first observation of the $Zn(OH)_2$ synthesis redirection towards ZnO where the agent was a dopant ion instead of a synthesis or post-synthesis parameter such as temperature, pressure or stirring. The systematic investigation of the samples prepared without Mn^{2+} and with Mn^{2+} ions in a wide nominal concentrations range showed that the synthesis redirection takes place for a Mn^{2+} nominal concentration as low as 1 ppm.

We have also found out that this effect takes place only for $Zn(OH)_2$, while the synthesis of other M(II) hydroxides (M(II) = Ca^{2+}, Mg^{2+}, Cd^{2+}) by the same procedure is not affected by the presence of a Mn source in the starting material. A possible explanation for the synthesis redirection from $Zn(OH)_2$ towards nano-ZnO is based on the different coordination properties of the Mn^{2+} and Zn^{2+} ions, which could lead to a coordinative hindrance for the Mn^{2+} ions.

We have also examined the extent of the manganese influence on the synthesis products. EPR investigations showed a non-uniform distribution of the Mn^{2+} ions in the resulting nano-ZnO samples. Besides the Mn^{2+} ions substitutionally localized in tetrahedrally coordinated Zn^{2+} sites in nanocrystalline and disordered ZnO, a significant amount of Mn^{2+} ions are segregated in a disordered secondary phase. FTIR investigations showed that this secondary phase could consist of rests of nitrate compounds from the precursors, in an amount below the detection limit of XRD. It was also found out that the percentage of segregated Mn^{2+} ions from the total concentration of Mn^{2+} ions incorporated in the samples decreases with the nominal concentration increase, while the percentage of Mn^{2+} ions localized in ZnO nanocrystals increases.

TEM and FTIR investigations evidenced morphological changes of the ZnO nanostructures associated with the Mn concentration increase. This result points to an interesting possibility to control the morphology and size of the ZnO nanostructures by varying the doping concentration, which is important for designing ZnO nanoparticles with high surface area for specific applications, such as catalysis or gas sensing.

We believe that this subject merits further experimental and theoretical investigations not least because, in the end, it provides a simple, cost and time effective, non-toxic method of preparation for manganese doped ZnO, with controlled morphology and particle size.

Acknowledgements

This work was supported by ANCS, Core Program project number PN16-480102 and by a grant of the Romanian National Authority for Scientific Research and Innovation, CNCS – UEFISCDI, project number PN-II-RU-TE-2014-4-0939.

References

1 U. Ozgur, Y. I. Alivov, C. Liu, A. Teke, M. A. Reshchikov, S. Dogan, V. Avrutain, S.-J. Cho and H. Morkoç, A comprehensive review of ZnO materials and devices, *J. Appl. Phys.*, 2005, **98**, 041301.

2 L. Schmidt-Mende and J. L. MacManus-Driscoll, ZnO – nanostructures, defects, and devices, *Mater. Today*, 2007, **10**, 40–48.

3 E. Fortunato, A. Gonçalves, A. Pimentel, P. Barquinha, G. Gonçalves, L. Pereira, I. Ferreira and R. Martins, Zinc oxide, a multifunctional material: from material to device applications, *Appl. Phys. A: Mater. Sci. Process.*, 2009, **96**, 197–205.

4 R. L. Z. Hoye, K. P. Musselman and J. L. MacManus-Driscoll, Research update: doping ZnO and TiO_2 for solar cells, *APL Mater.*, 2013, **1**, 060701, and references cited therein.

5 S. C. Erwin, L. Zu, M. I. Haftel, A. L. Efros, T. A. Kennedy and D. J. Norris, Doping semiconductor nanocrystals, *Nature*, 2005, **436**, 91–94.

6 D. J. Norris, A. L. Efros and S. C. Erwin, Doped nanocrystals, *Science*, 2008, **319**, 1776–1779.

7 S. V. Nistor, M. Stefan, L. C. Nistor, D. Ghica, I. D. Vlaicu and A. C. Joita, Doping ultrasmall cubic ZnS nanocrystals with Mn^{2+} ions over a broad nominal concentration range, *J. Phys. Chem. C*, 2015, **119**, 23781–23789.

8 S. V. Nistor, L. C. Nistor, M. Stefan, D. Ghica, G. Aldica and J. N. Barascu, Crystallization of disordered nanosized ZnO formed by thermal decomposition of nanocrystalline hydrozincite, *Cryst. Growth Des.*, 2011, **11**, 5030–5038.

9 M. Stefan, S. V. Nistor and D. Ghica, Correlation of lattice disorder with crystallite size and the growth kinetics of Mn^{2+} doped ZnO nanocrystals probed by Electron Paramagnetic Resonance, *Cryst. Growth Des.*, 2013, **13**, 1350–1359.

10 R. A. McBride, J. M. Kelly and D. E. McCormack, Growth of well-defined ZnO microparticles by hydroxide ion hydrolysis of zinc salts, *J. Mater. Chem.*, 2003, **13**, 1196–1201.

11 S. Music, D. Dragcevic and S. Popovic, Influence of synthesis route on the formation of ZnO particles and their morphologies, *J. Alloys Compd.*, 2007, **429**, 242–249.

12 M. Wang, Y. Zhou, Y. Zhang, S. H. Hahn and E. J. Kim, From $Zn(OH)_2$ to ZnO: a study on the mechanism of phase transformation, *CrystEngComm*, 2011, **13**, 6024–6026.

13 S. V. Nistor, D. Ghica, M. Stefan, I. Vlaicu, J. N. Barascu and C. Bartha, Magnetic defects in crystalline $Zn(OH)_2$ and nanocrystalline ZnO resulting from its thermal decomposition, *J. Alloys Compd.*, 2013, **548**, 222–227.

14 F. Demoisson, R. Piolet and F. Bernard, Hydrothermal synthesis of ZnO crystals from $Zn(OH)_2$ metastable phases at room to supercritical conditions, *Cryst. Growth Des.*, 2014, **14**, 5388–5396.

15 Z. Mickovic, D. T. L. Alexander, A. Sienkiewicz, M. Mionic, L. Forro and A. Magrez, Synthesis of nanosized Mn-doped ZnO by low temperature decomposition of hydrozincite precursors, *Cryst. Growth Des.*, 2010, **10**, 4437–4441.

16 A. Top and H. Cetinkaya, Zinc oxide and zinc hydroxide formation *via* aqueous precipitation: effect of the preparation route and lysozyme addition, *Mater. Chem. Phys.*, 2015, **167**, 77–87.

17 D. Ghica, M. Stefan, C. Ghica and G. E. Stan, Evaluation of the paramagnetic impurities segregation at grain boundaries in nanostructured ZnO films, *ACS Appl. Mater. Interfaces*, 2014, **6**, 14231–14238.

18 M. Stefan, D. Ghica, S. V. Nistor, A. V. Maraloiu and R. Plugaru, Mn^{2+} ions distribution in doped sol-gel deposited ZnO films, *Appl. Surf. Sci.*, 2016, DOI: 10.1016/j.apsusc.2016.02.167.

19 S. V. Nistor, D. Ghica, M. Stefan and L. C. Nistor, Sequential thermal decomposition of the shell of cubic $ZnS/Zn(OH)_2$ core-shell quantum dots observed with Mn^{2+} probing ions, *J. Phys. Chem. C*, 2013, **117**, 22017–22028.

20 M. Stefan, S. V. Nistor and J. N. Barascu, Accurate determination of the spin Hamiltonian parameters for Mn^{2+} ions in cubic ZnS nanocrystals by multifrequency EPR spectra analysis, *J. Magn. Reson.*, 2011, **210**, 200–209.

21 S. Stoll and A. Schweiger, EasySpin, a comprehensive software package for spectral simulation and analysis in EPR, *J. Magn. Reson.*, 2006, **178**, 42–55.

22 R. D. Shannon, Revised effective ionic radii and systematic studies of interatomic distances in halides and chalcogenides, *Acta Crystallogr., Sect. A: Cryst. Phys., Diffr., Theor. Gen. Crystallogr.*, 1976, **32**, 751–767.

23 A. Michels, C. E. Krill, H. Erhardt, R. Birringer and D. T. Wu, Modelling the influence of grain-size-dependent solute drag on the kinetics of grain growth in nanocrystalline materials, *Acta Mater.*, 1999, **47**, 2143–2152.

24 B. Ingham, R. Linklater and T. Kemmitt, Grain growth kinetics of ZnO: Al nanocrystalline powders during calcination from sol-gel, *J. Phys. Chem. C*, 2011, **115**, 21034–21040.

25 R. Karmakar, S. K. Neogi, A. Banerjee and S. Bandyopadhyay, Structural, morphological, optical and magnetic properties of Mn doped ferromagnetic ZnO thin film, *Appl. Surf. Sci.*, 2012, **263**, 671–677.

26 M. Diaconu, H. Schmidt, A. Poeppl, R. Bottcher, J. Hoentsch, A. Klunker, D. Spemann, H. Hochmuth, M. Lorenz and M. Grundmann, Electron paramagnetic resonance of $Zn_{1-x}Mn_xO$ thin films and single crystals, *Phys. Rev. B: Condens. Matter Mater. Phys.*, 2005, **72**, 085214.

27 E. Simanek and K. A. Muller, Covalency and hyperfine structure constant *A* of iron group impurities in crystals, *J. Phys. Chem. Solids*, 1970, **31**, 1027–1040.

28 N. Tsujii, H. Kitazawa and G. Kido, Magnetic properties of Mn- and Eu-doped ZnS nanocrystals, *J. Appl. Phys.*, 2003, **93**, 6957–6959.

29 R. M. Krsmanovic Whiffen, D. J. Jovanovic, Z. Antic, B. Bartova, D. Milivojevic, M. D. Dramicanin and M. G. Brok, Structural, optical and crystal field analyses of undoped and Mn^{2+} - doped ZnS nanoparticles synthesized *via* reverse micelle route, *J. Lumin.*, 2014, **146**, 133–140.

30 S. Bhattacharyya, D. Zitoun and A. Gedanken, Electron paramagnetic resonance spectroscopic investigation of manganese doping in ZnL (L = O, S, Se, Te) nanocrystals, *Nanosci. Nanotechnol. Lett.*, 2011, **3**, 541–549.

31 S. V. Nistor, M. Stefan, L. C. Nistor, D. Ghica and I. D. Vlaicu, Distribution and interaction of Mn^{2+} ions incorporated in cubic ZnS quantum dots over a broad concentration range, *J. Alloys Compd.*, 2016, **662**, 193–199.

32 T. Singh, T. J. Mountziaris and D. Maroudas, On the transition-metal doping efficiency of zinc oxide nanocrystals, *Appl. Phys. Lett.*, 2010, **97**, 073120.

33 M. Andrés Vergés, A. Mifsud and C. J. Serna, Formation of rod-like zinc oxide microcrystals in homogeneous solutions, *J. Chem. Soc., Faraday Trans.*, 1990, **86**, 959–963.

34 F. A. Sigoli, M. R. Davolos and M. Jafelicci, Morphological evolution of zinc oxide originating from zinc hydroxide carbonate, *J. Alloys Compd.*, 1997, **262–263**, 292–295.

35 J. Coates, Interpretation of infrared spectra, a practical approach, in *Encyclopedia of Analytical Chemistry*, ed. R. A. Meyers, Wiley and Sons Ltd., Chichester, 2000, pp. 10815–10837.

36 K. Nakamoto, *Infrared and Raman Spectra of Inorganic and Coordination Compounds*, Wiley, New York, 1986.

37 L. C. Nistor, C. D. Mateescu, R. Birjega and S. V. Nistor, Synthesis and characterization of mesoporous ZnS with narrow size distribution of small pores, *Appl. Phys. A: Mater. Sci. Process.*, 2008, **92**, 295–301.

38 A. K. Guria and N. Pradhan, Doped or not doped: ionic impurities for influencing the phase and growth of semiconductor nanocrystals, *Chem. Mater.*, 2016, **28**, 5224–5237.

39 K. Jayanthi, S. Chawla, K. N. Sood, M. Chhibara and S. Singh, Dopant induced morphology changes in ZnO nanocrystals, *Appl. Surf. Sci.*, 2009, **255**, 5869–5875.

40 Y. Yang, Y. Jin, H. He, Q. Wang, Y. Tu, H. Lu and Z. Ye, Dopant-induced shape evolution of colloidal nanocrystals: the case of zinc oxide, *J. Am. Chem. Soc.*, 2010, **132**, 13381–13394.

41 J. Iqbal, T. Jan, Y. Ronghai, S. H. Naqvi and I. Ahmad, Doping induced tailoring in the morphology, band-gap and ferromagnetic properties of biocompatible ZnO nanowires, nanorods and nanoparticles, *Nano-Micro Lett.*, 2014, **6**, 242–251.

42 C. Fletcher, Y. Jiang, C. Sun and R. Amal, Morphological evolution and electronic alteration of ZnO nanomaterials induced by Ni/Fe co-doping, *Nanoscale*, 2014, **6**, 7312–7318.

43 P. M. Shirage, A. K. Rana, Y. Kumar, S. Sen, S. G. Leonardi and G. Neri, Sr- and Ni-doping in ZnO nanorods synthesized by a simple wet chemical method as excellent materials for CO and CO_2 gas sensing, *RSC Adv.*, 2016, **6**, 82733–82742.

44 N. Fujimura, T. Nishihara, S. Goto, J. Xu and T. Ito, Control of preferred orientation for ZnO_x films: control of self-texture, *J. Cryst. Growth*, 1993, **130**, 269–279.

45 Y. Yang, Y. Li, L. Zhu, H. He, L. Hu, J. Huang, F. Hu, B. He and Z. Ye, Shape control of colloidal Mn doped ZnO nanocrystals and their visible light photocatalytic properties, *Nanoscale*, 2013, **5**, 10461–10471.

46 W. A. Pieczonka, H. E. Petch and A. B. McLay, An electron spin resonance study of manganese impurity in brucite, *Can. J. Phys.*, 1961, **39**, 145–157.

47 F. Holuj, S. M. Quick and M. Rosen, Vibronic effects in the electron paramagnetic resonance of Mn^{2+} in $Ca(OH)_2$, *Phys. Rev. B: Condens. Matter Mater. Phys.*, 1972, **6**, 3169–3179.

48 L. Guerlou-Demourgues and C. Delmas, Electrochemical behavior of the manganese-substituted nickel hydroxides, *J. Electrochem. Soc.*, 1996, **143**, 561–566.

49 M. Morishita, S. Ochiai, T. Kakeya, T. Ozaki, Y. Kawabe, M. Watada, S. Tanase and T. Sakai, Structural analysis by synchrotron XRD and XAFS for manganese-substituted α - and β -type nickel hydroxide electrode, *J. Electrochem. Soc.*, 2008, **155**, A936–A944.

50 R. Wahab, S. G. Ansari, Y. S. Kim, M. Song and H.-S. Shin, The role of pH variation on the growth of zinc oxide nanostructures, *Appl. Surf. Sci.*, 2009, **255**, 4891–4896.

51 A. Bagabas, A. Alshammari, M. F. A. Aboud and H. Kosslick, Room-temperature synthesis of zinc oxide nanoparticles in different media and their application in cyanide photodegradation, *Nanoscale Res. Lett.*, 2013, **8**, 516.

52 A. M. Pourrahimi, D. Liu, L. K. H. Pallon, R. L. Andersson, A. Martinez Abad, J.-M. Lagaron, M. S. Hedenqvist, V. Strom, U. W. Gedde and R. T. Olsson, Water-based synthesis and

cleaning methods for high purity ZnO nanoparticles – comparing acetate, chloride, sulphate and nitrate zinc salt precursors, *RSC Adv.*, 2014, **4**, 35568–35577.

53 M. F. Khan, A. H. Ansari, M. Hameedullah, E. Ahmad, F. M. Husain, Q. Zia, U. Baig, M. R. Zaheer, M. M. Alam, A. M. Khan, Z. A. AlOthman, I. Ahmad, G. Md Ashraf and G. Aliev, Sol-gel synthesis of thorn-like ZnO nanoparticles endorsing mechanical stirring effect and their antimicrobial activities: Potential role as nano-antibiotics, *Sci. Rep.*, 2016, **6**, 27689.

54 J. P. Glusker, A. Kaufman Katz and C. W. Bock, Metal ions in biological systems, *Rigaku J.*, 1999, **16**, 8–16.

55 C. W. Bock, A. Kaufman Katz, G. D. Markham and J. P. Glusker, Manganese as a replacement for magnesium and zinc: functional comparison of the divalent ions, *J. Am. Chem. Soc.*, 1999, **121**, 7360–7372.

56 I. Herber, W.-K. Tang, H.-Y. Wong, T.-W. Lam, C.-K. Siu and M. K. Beyer, Reactivity of hydrated monovalent first row transition metal ions $[M(H_2O)_n]^+$, M = Cr, Mn, Fe, Co, Ni, Cu, and Zn, n < 50, toward acetonitrile, *J. Phys. Chem. A*, 2015, **119**, 5566–5578.

57 E. A. Meulenkamp, Synthesis and growth of ZnO nanoparticles, *J. Phys. Chem.*, 1998, **102**, 5566–5572.